

## Near-source Ground Motion of a Propagating Rupture Fault From the Finite Element Modeling

BOR-SHOUH HUANG<sup>1</sup> and YEONG TEIN YEH<sup>1,2</sup>

(Manuscript received 10 December 1993, in final form 10 May 1994)

### ABSTRACT

A finite element algorithm was developed to simulate wave propagation and near-source ground motion of propagating rupture fault. The modified 'split-node' technique of Melosh and Raefsky was employed to simulate the equivalent body forces system for a double couple without moment. Synthetic seismograms were computed for a suite of dip-slip faultings with various slip directions, and rupture velocities to illustrate the ground motion and coseismic deformation variations. Results from this study showed that, for a thrust fault with infinite rupture velocity or down going propagating ruptures, the hanging wall has a stronger ground motion than the foot wall; in contrast, for up going or bi-lateral ruptures, the hanging wall has a weaker shaking than foot wall. For the propagating rupture faults, the 'starting' and 'stopping' phases were numerically reproduced using the finite element method. In addition, observation at the surface, the duration pulse of S-waves were significantly changed between both sides of the fault for the rupture directivity.

(Key words: Finite element, Near-source ground motion, Source rupture, Wave form)

### 1. INTRODUCTION

The study of earthquake sources is one of the prime concerns for seismologist. The bulk of knowledge about earthquake sources comes from research through practical observation and theoretical investigations. Theoretical study of the earthquake source rupture process was previously published by Haskell (1969) to compute the ground motion of finite tensile fault. Boore and Zoback (1974) computed the near-source motion of the inplane finite rupture, while Madariaga (1976) computed the dynamic rupture of circular fault using the finite difference method. Previous theoretical near-source ground motion modeling has typically been restricted to full-space (Luco and Sotiropoulos, 1985) and constant propagation rupture (Bouchon, 1980) models. The application of these methods did, indeed, successfully interpret records from the 1966 Parkfield earthquake (Aki, 1968) and the 1979 Imperial

<sup>1</sup> Institute of Earth Sciences, Academia Sinica, P.O. Box 1-55, Nankang, Taipei, Taiwan, R.O.C.

<sup>2</sup> Institute of Seismology, National Chung Cheng University, Minhsiung, Chiayi, Taiwan, R.O.C.

Valley earthquake (Archuleta, 1984). In addition, many studies related to source rupture were proposed (Goldstein and Archuleta, 1991; Chiu, 1991), but their results showed that the source rupture process and fault geometry are more complex than those from teleseismic observation. They demonstrated the fact that the detailed source rupture processes may be retrieved from the near-source strong motion simulation (Hartzell and Heaton, 1983; Wald *et al.*, 1991). However, the resolutions from those studies were limited due to combined effects from the laterally varying velocity structure, topographic effects, attenuation and anisotropy. Other than this, detailed knowledge about near-source ground motion behavior is still not well define. Recently, the installation of digital strong motion and broad-band instruments have acquired a great deal of high quality seismic data (Abrahamson *et al.*, 1987; CDMG, 1989; Kanamori *et al.*, 1991; Helmberger *et al.*, 1993), thereby creating new opportunities to improve the knowledge of source rupture processes. Nevertheless, to extract the source information from near-source observation, accurate wave-form modeling is necessary.

The finite element method, which is well known as a robust numerical method for synthetic seismogram simulation, is one of the modeling techniques for the study of the near-source ground motion behavior because of its natural ability to simulate both complex elastic models and complex sources. Many complex structure can be easily modeled using the finite element method without difficult modifications to the algorithm (Zienkiewicz, 1977). Moreover, the method can be easily employed to approximate the topography. In this study, the authors presented the finite element method to model the ground motion from the fault rupture. Also, the 'split-node' technique (Melosh and Raefsky, 1981) was employed to simulate a complex dislocation rupture source. Although it is not presented in this study, however, this approach lent itself as a possible tool for the complete wave form modeling of complex source geometry and slip distribution in a laterally varying velocity structure. In this study, the near-source ground motion computed from the numerical modeling was analyzed. The results of this study showed that rupture velocity changes have strong effect on the near field ground motions.

## 2. METHOD

### 2.1 Finite Element Formulation

In the finite element method, wave motion due to external loading force can be described as a set of simultaneous, second-order differential equations results:

$$[M][A] + [C][V] + [K][D] = [F] \quad (1)$$

where  $[M]$  is the global mass matrix,  $[C]$  is the damping matrix, and  $[K]$  is the global stiffness matrix.  $[A]$ ,  $[V]$  and  $[D]$  are the vectors of the global acceleration, velocity and displacement of the model at grid points.  $[F]$  is the vector of the external loading forces at source points. The medium properties with lateral variation can be easily specified within the model. In this study, a transient method is applied to solve equation (1) for the displacements at each node. We used the explicit finite difference approximations (Wylie, 1975):

$$[V^{(t+1/2\Delta t)}] = [V^{(t-1/2\Delta t)}] + \Delta t[A^{(t)}]$$

and

$$[D^{(t+D\Delta t)}] = [D^{(t)}] + \Delta t[V^{(t+1/2\Delta t)}] \quad (2)$$

where  $\Delta t$  is the time interval used in numerical integration. Results from the finite element computation are the full solution of propagating waves; thus, all transmitted and reflected waves, converted waves, surface waves, diffraction, head waves and multiple scattered waves are included.

## 2.2 Fault Dislocation Formulation

Melosh and Raefsky (1981) proved that the static rupture fault may be implemented as an equivalent double-couple force distribution without moment. As a result, they developed a split-node technique to represent the fault dislocation (equation (7) in Melosh and Raefsky, 1981):

$$[K][D] = [F] \quad (3)$$

In this study, the 'split-node' technique was extended to simulate the dynamic dislocation rupture processes via solution of the elastic wave equation. In this case, the static forces  $[F]$  used in equation (3) were replaced by the dynamic forces  $[F(t)]$  which were represented as ramp functions (Figure 1) to simulate the rupture propagation by suitable time delays (Yeh and Huang, 1986; Huang, 1989). Similarly, the static deformation  $[D]$  in equation (1) was replaced as seismogram  $[D(t)]$  at each node.

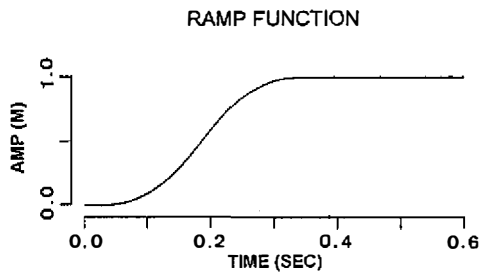


Fig. 1. The ramp type displacement source time function which is used in all cases of this study.

## 2.3 Numerical Implementation

The 2-dimensional, 4-node quadrilateral element was used in this study to modeling wave propagation. For handling the fault plane which slips across the elements, the local assemblage technique to redistribute the equivalent forces to grids was used (Zienkiewicz, 1977). To keep numerical dispersion down to an acceptable level, the grid interval which was less than one over ten wavelengths of the dominant frequency of the S wave was selected. A damping matrix  $[C]$  was used with a damping coefficient as defined by Archuleta and Frazier (1978) in the 0.1 to 0.2 range. The increasing of the damping coefficient will reduce the ringing with calculated signals, however, it also reduces the signal amplitudes. There is not a suitable theory to select the damping coefficient, the authors suggested a trial and error test in each case. In order to suppress numerical reflections from the artificial boundaries of the finite element model, the boundary absorbing method proposed by Smith (1974) was used. This method involved the superposition of independently calculated wave equation solutions with Neumann and Dirichlet conditions. Although the method proposed by Smith (1974) can not cancel the multiple reflections between free surface and artificial boundaries,

however, primary and corner reflections may completely cancel using this method (see Figure 1 of Huang and Yeh, 1991). A similar procedure for source rupture processes was proposed by Benz and Smith (1987) to model the source rupture. For the purpose of comparing the accuracy of both algorithms, a case proposed by Benz and Smith (1987) was reproduced and is shown in Figure 2. Nearly the same amplitudes and wave forms are present in both profiles. The difference in artificial boundary reflection, noted as BR in Figure 2, may be due to different numerical approximations. Otherwise, the code in this study was checked against with the analytic solution (Huang, 1992) and the pseudo-spectral method (Huang and Yeh, 1991).

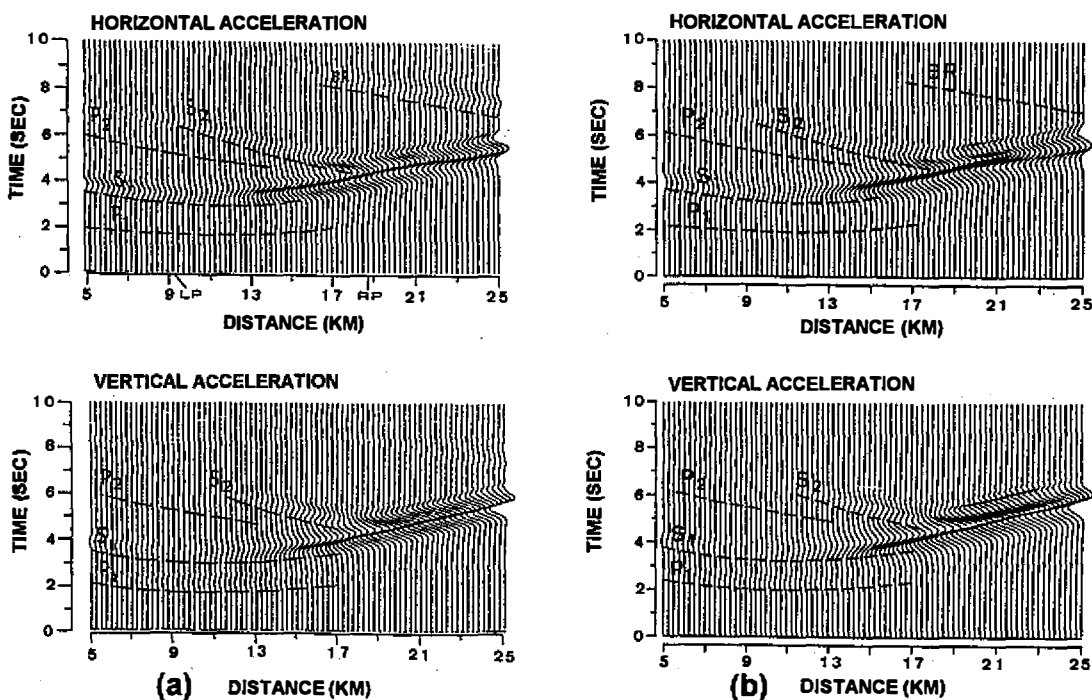


Fig. 2. Comparison of seismic profiles computed by Benz and Smith (1987) (a) and this study (b). The dashed lines noted as BR are the arrival times of the boundary reflection phases, P1 and S1 are arrival times of the 'starting phases' of P and S waves, while P2 and S2 are the arrival times of the 'stopping phases'.

### 3. SYNTHETIC EXAMPLES

This study demonstrated two numerical experiments to simulate near-source ground motion. First, we computed the near-source ground motion features for the model size near 14 times that of the fault dimension (Experiment 1). In this case, the fault was simulated by 12 grid points. The second model on which the rupture fault was discretized by 90 grid points. In this experiment, the dimension of the model is about 2 times larger than the fault dimension. The detailed properties of the rupture directivity and rupture complexity were examined.

### 3.1 Experiment 1

The goal of this experiment was to analyze the amplitude characteristics of ground motion from finite source with a propagating rupture process. For this purpose, a model of  $45^\circ$  dip-slip thrust fault on half-space was used and was shown in Figure 3. The ground motion recorded on the free surface (Figure 4) and wavefield snapshots (Figure 5) were examined. The definition of the positive direction of seismograms in Figure 4 is up for the vertical component and right for the horizontal component. The definition remains the same in the other figures of this study. In Figure 4, the vertical acceleration profile has simple wave forms, except for the small range near the fault tip on which the surface waves were interfered by the propagating waves at free surface. The ground motion on the hanging wall have stronger shaking and more complex wave forms than that on the foot wall. Most of the energy which propagated to the left was downward and away from the free surface. Major contribution of energy are from scattering from fault tip. The integrated vertical velocity and displacement seismograms of Figure 4 have similar characteristics as shown in Figure 6 except lower frequencies. The vertical displacement on the foot wall was subsidence while on the hanging wall it was lift. For the displacement ramp type source time function used in this study to modeling the dislocation rupture, the permanent deformation which show the final offset of the fault rupture can be measured in each end of the seismograms of the displacement profile (Figure 6(b)). Along the profile on the free surface, the permanent deformation is shown in Figure (7).

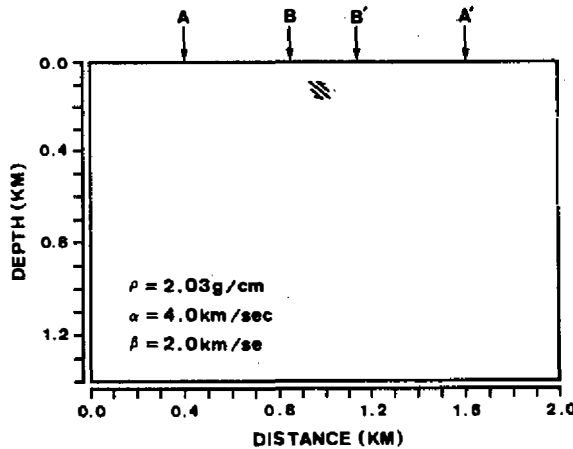


Fig. 3. The half-space model used in Experiment 1 of this study. The depth of the upper fault tip is 120 m; the dip angle is  $45^\circ$ . Only the central part, thus AA', with a range of 1.2 km was selected in the future display.

A model with the same fault geometry as in Figure 3 but as a bi-lateral propagating rupture is proposed to demonstrate the amplitude characteristics of ground motion. A source time function (Figure 8) was chosen to compute the synthetic seismograms to demonstrate the difference between the bi-lateral and the infinite rupture sources (Figure 4). In this case, the rupture was initiated at the center of fault plane then propagated to two ends. Although the fault type (thrust fault) is the same as the infinite rupture case, however, the free surface

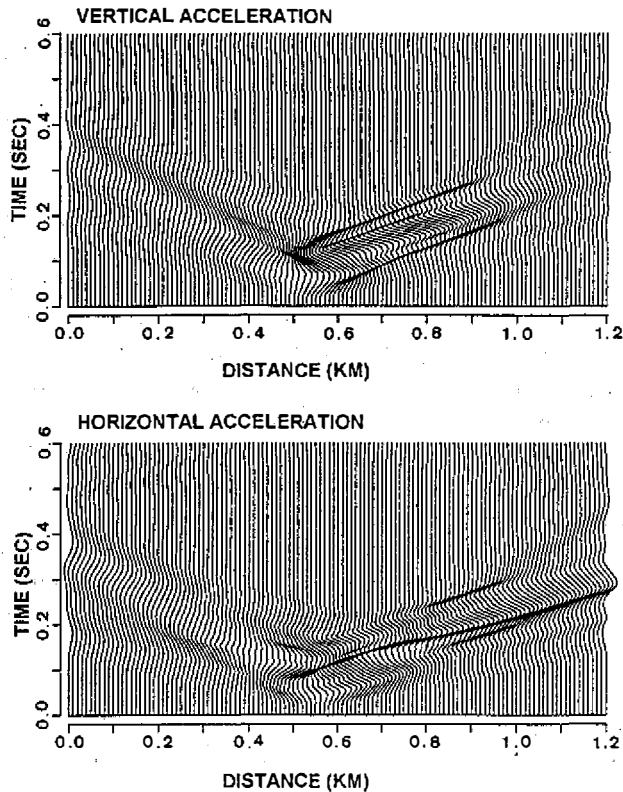


Fig. 4. Acceleration profiles of the ground surface of Experiment 1. The fault geometry is shown in Figure 3.

ground motion of the propagating rupture has a complex time history than a infinite rupture velocity case (Figure 4) as shown in Figure 9. In the bi-lateral rupture case, the shaking on the foot wall have larger values than that on the hanging wall. The frequency content of the horizontal acceleration seismograms on foot wall is higher than that on the hanging wall. The detailed seismograms recorded at location 0.57 km for different rupture process are shown in Figure 10. The seismogram of the bi-lateral propagating fault on this point shows a complex wave form but a small peak amplitude than that of the infinite rupture velocity case.

### 3.2 Experiment 2

For a detailed study of the wave form features near and above the rupture fault, a thrust slip model of a large fault dimension, a model as shown in Figure 11 was proposed. Figure 12 shows the acceleration seismograms of a dip-slip faulting with constant rupture velocity. This case presents a upward propagating rupture from the lower end tip (point A) to the upper end tip (point B) with a rupture velocity ( $V_r$ ) equal to 0.8 S-wave velocity ( $V_s$ ). The solid lines on Figure 12 represent the predicted P-wave (P1) and S-wave (S1) arrival times for the starting phase, and P2 and S2 for the stopping phases. The S-waves have larger amplitudes than P-waves in both vertical and horizontal components. S1 is separated from the S2 on the hanging wall. On the foot wall near the upper fault tip, the phase S1 and S2 arrived nearly at the same time. In this case, the direction of rupture propagation is toward left. The effects of

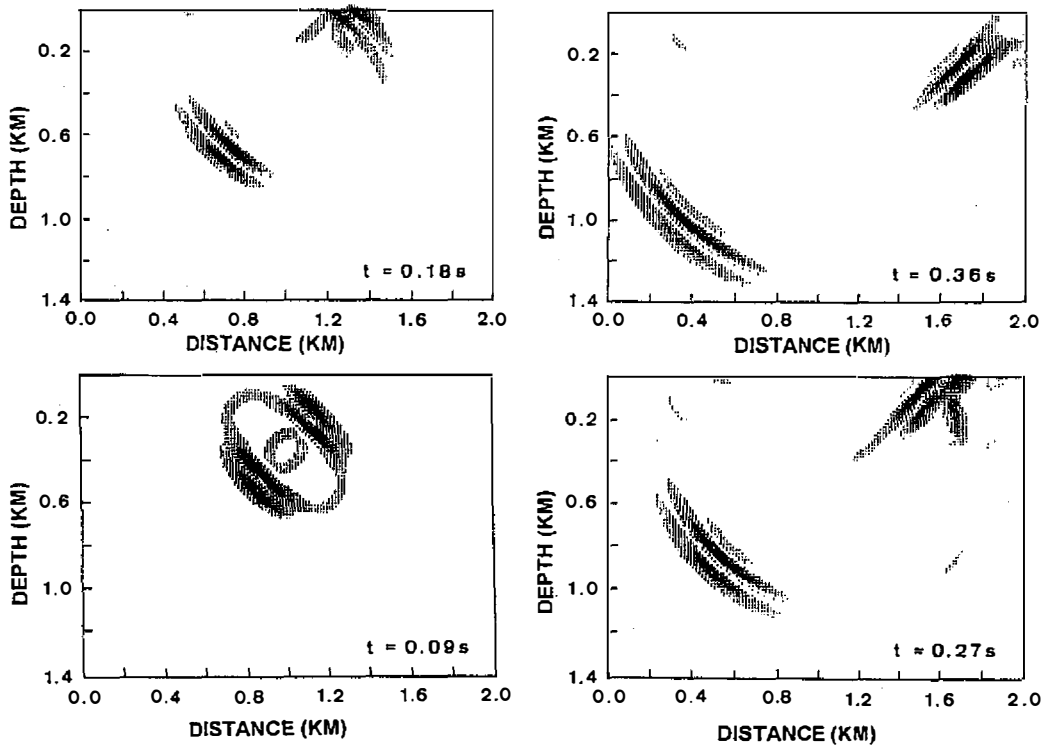


Fig. 5. Acceleration snapshots of the model of Figure 3 with an infinite rupture velocity. The elastic wavefields are expressed in a vector format.

directivity corresponding to large amplitudes and more coherent signal can be clearly seen on the seismograms at the left hand side of the fault tip as shown in Figure 12. The free surface ground motions at locations which are indicated as LP, MP and RP on Figure 11 are shown in Figure 13. From the acceleration seismograms, phases P2, S1 and S2 arrived at LP nearly the same time and produced a single pulse with a peak amplitude larger than RP and MP. However, phases P1 and S1 were clearly separated from P2, S2 at RP. For the pure dip-slip faulting of this case, the vertical acceleration on point LP was strongly enhanced. Although the peak amplitude ratio of LP/RP on a vertical displacement is 3, but, the ratio for vertical acceleration is up to 14. However, the amplitude enhanced on the horizontal component is not as clear as on the vertical one with horizontal displacement ratio as 2.5 and horizontal acceleration ratio as 5.1.

Figure 14 shows the seismic profiles of a pure thrust fault with downward propagated rupture which has the same fault geometry as in Figure 11 but the rupture initiated from point B with downward propagation ( $V_r = 0.8 V_s$ ) to point A. In this case, the directivity is not as clear as the upward propagation (Figure 12). From the acceleration profiles, the arriving phases P2 and S2 can be clearly separated from P1 and S1 on both side of fault. However, larger amplitudes and shorter duration were found on the hanging wall of the fault.

Selected seismograms at point MP of Figure 11 for both rupture faulting types are shown in Figure 15. The ground motion amplitude of upward propagated faulting is larger than that from the downward propagated faulting. The total duration (from P1 to S2) of upward propagation faulting is shorter than that of the downward propagation faulting. In

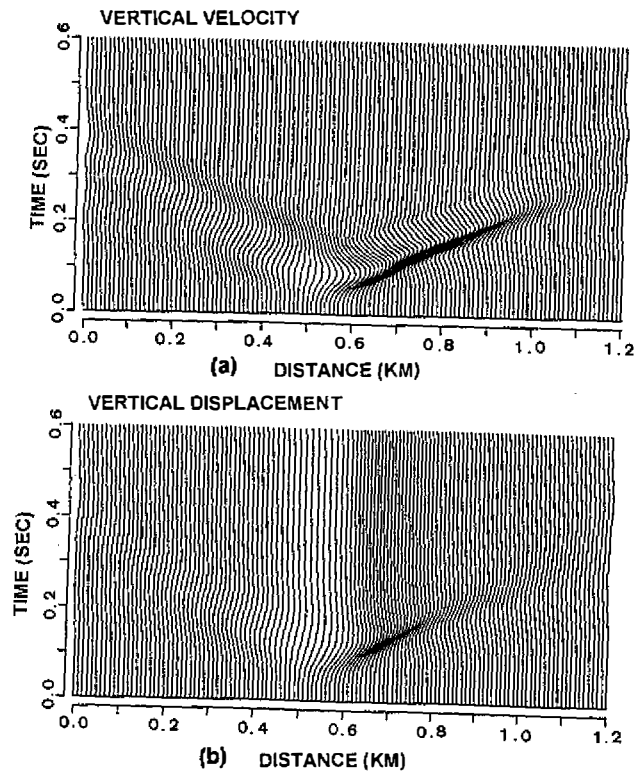


Fig. 6. The vertical seismic profiles of (a). velocity and (b). displacement of the same model of Figure 3. The profile observed range was the same as in Figure 4.

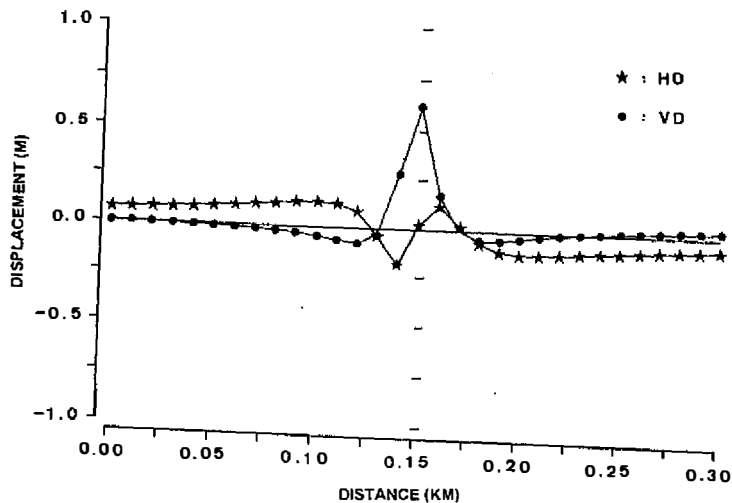


Fig. 7. The displacement profile of the final offset of the model of Figure 3 with infinite rupture velocity. HD represented the horizontal displacement, while VD the vertical. Only on the range of 0.3 km on Figure 3, thus BB', which centered on the upper fault tip was selected in this profile.

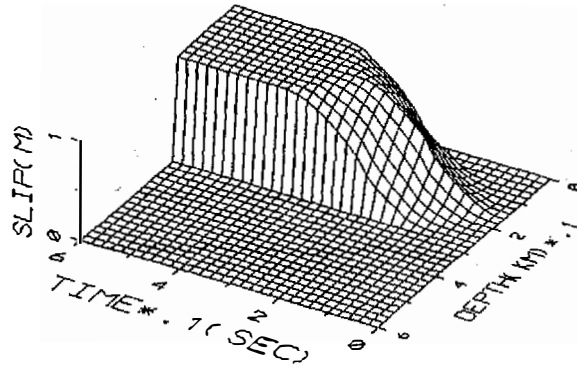


Fig. 8. The space-time diagram of the source slip time function of the bi-lateral rupture fault used in this study. The fault geometry was the same as in Figure 3.

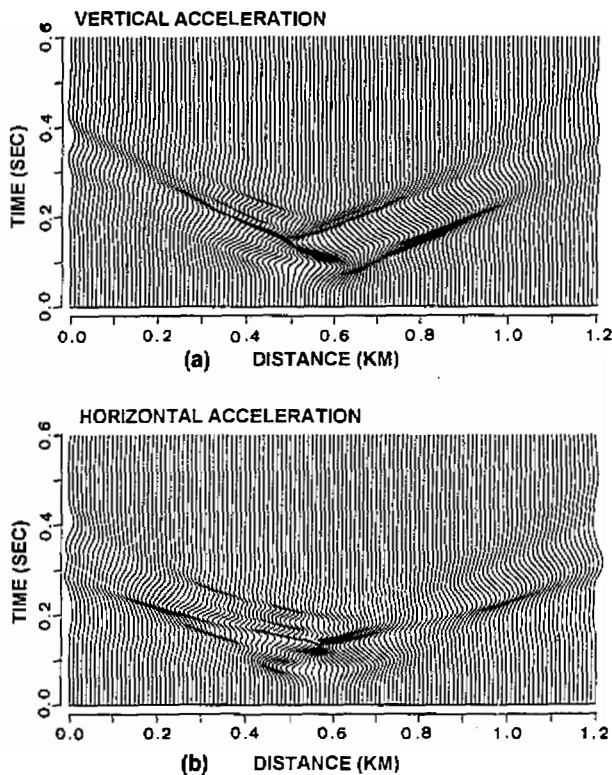


Fig. 9. Acceleration profiles of the bi-lateral rupture model (Figure 8) on the free surface. (a). vertical and (b). horizontal acceleration seismograms. In this case, the value of the rupture velocity is assumed to have a 0.8 S-wave velocity.

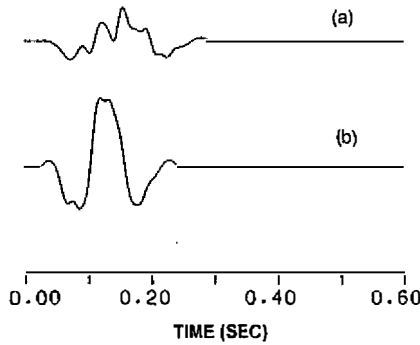


Fig. 10. Comparison of the horizontal acceleration seismograms for different rupture velocities. (a).  $V_r=0.8 V_s$  and bi-lateral rupture, (b).  $V_r=infty$ . Both seismograms were recorded at 0.57 km of Figure 4.

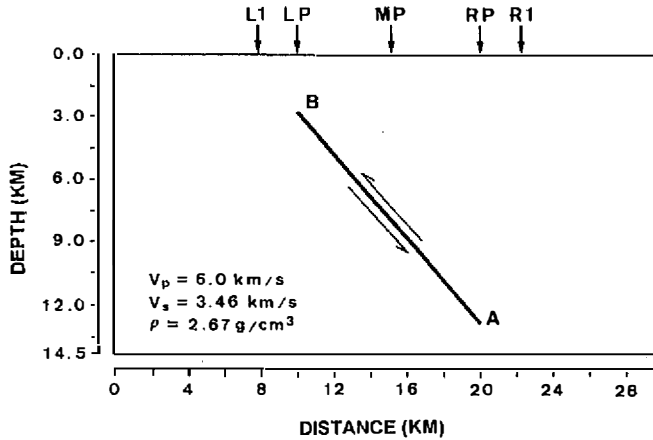


Fig. 11. The half-space model used in Experiment 2 of this study. The source was a  $45^\circ$  dip-slip thrust fault. Character A represents the lower tip of the fault while B the upper tip. LP, MP and RP represent the location of the projection of the fault left end, middle point and right end of the fault. The depth of the upper fault tip was 3 km.

both cases, the arrival phases of P and S waves radiated within the fault segment (between point B and A) cannot be identified from those seismograms. The surface ground motions represented the low frequency features during the rupture front passing.

To demonstrate the difference in the recorded ground motions by changing the rupture velocity for the same fault geometry and propagating direction, in this study, we present two cases. Both cases are the upward propagating ruptures from point A of Figure 11 to point B. The first one, which is noted as ' $v^+$ ' case in Figure 16 and 17, increases the rupture velocities from 0.8 to 1.12 S wave velocity, uniformly. The other one, which is noted as ' $v^-$ ' case in Figure 16 and 17, decreases rupture velocity from 0.8 to 0.46 S wave velocity, uniformly. The ' $V_r$ ' case, which has the constant rupture velocity (0.8 S wave velocity) was discussed in Figure 12 and 13. We selected two observation point at L1 and R1 (Figure 11).

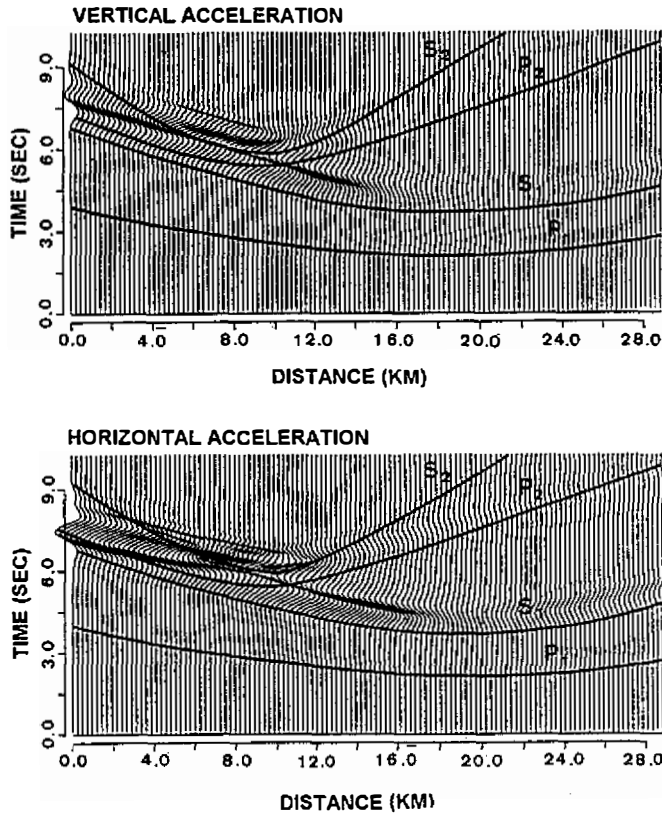


Fig. 12. Horizontal and vertical component synthetic acceleration seismograms for the fault model of Experiment 2 (Figure 11) with a uniform source rupture velocity (0.8 S-wave velocity) from the lower end (point A) upward propagating to the upper end (point B). P<sub>1</sub>, S<sub>1</sub> are the P-wave and S-waves which radiated from point A; P<sub>2</sub>, S<sub>2</sub> are the P and S-waves from point B.

L1 indicates the point of 2.5 km to the left of LP. R1 indicates the point of 2.5 km to the right of RP. Figure 16 and 17 shows the seismograms recorded at L1 and R1 for the ' $v^+$ ', ' $v^-$ ' and ' $v_r$ ' cases. Figure 16 show that in the beginning of the seismograms are similar among the three cases where as the later-phases have significantly changed. The ground motion was strongly amplified for the increasing rupture velocity case and deamplified for the decreasing rupture velocity case. The duration of seismograms for the  $v^+$  case is shorter than  $v_r$  or  $v^-$  case. For the  $v^+$  case, the P wave may be completely separated from the S wave on the acceleration seismograms, because P2 recorded early than S1. Although it is not a point source, the increasing rupture velocity case shows a very simple acceleration seismograms. The ground motion on the hanging wall, for example point R1 (Figure 17), shows a smaller amplitude value, for all of the attribute, than that on L1 (Figure 16) for the same case. At R1, the peak amplitudes of seismograms are similar for the rupture velocity change. The acceleration seismograms show clear P-arrival at R1 (Figure 17) than that at point L1 (Figure 16).

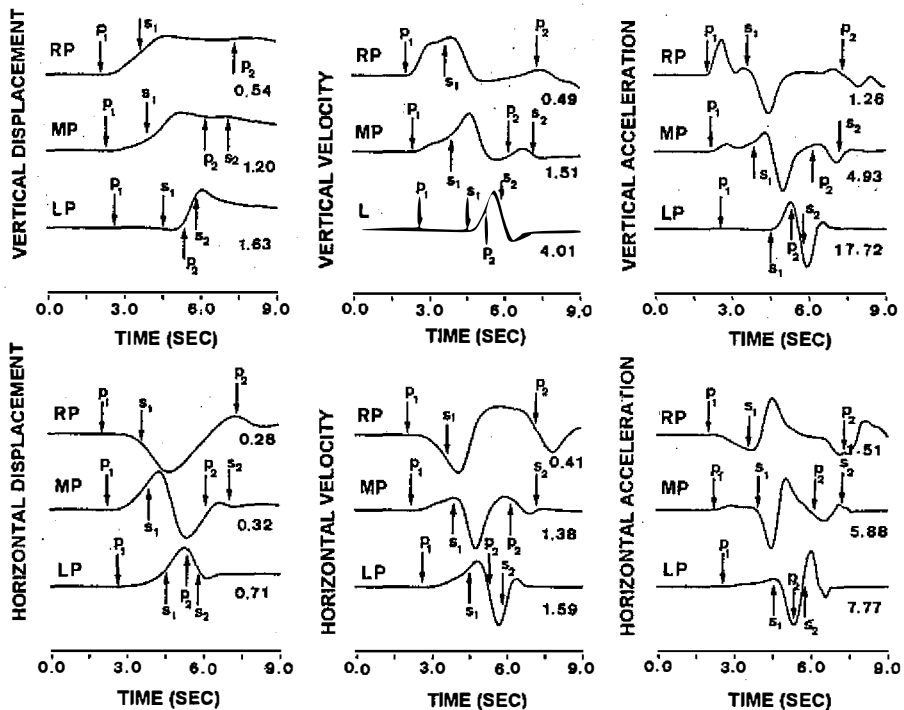


Fig. 13. Horizontal and vertical component synthetic acceleration, velocity and displacement seismograms on points LP, MP and RP of Figure 11. Identification symbols remain the same as in Figure 12. The number at the right end of each seismogram represents the peak value.

#### 4. DISCUSSION

The near source ground acceleration from the point dislocation source was found as a wave let type motion (Johnson, 1974). In this study, it was found that the ground motion from the finite instantaneous rupture fault was still similar to that from the point source as shown in Figure 4 and Figure 10 (b). However, the wave form was relatively complex for the bi-lateral rupture faulting, as shown in Figure 10 (a), and the unilateral rupture faulting as shown in Figure 13, 15, 16 and 17. Actually, the rupture effect in the source spectra has become known as directivity (Aki and Richards, 1980; Bullen and Bolt, 1985; Douglas *et al.*, 1988). Observations showed that the amplitudes and duration of the ground motion were different for the station on different azimuths of rupture sources (Hartzell, 1989; Ammon *et al.*, 1992). However, most theoretical discussions for the directivity were only for frequency domain features (Haskell, 1964; Hasegawa, 1974) and the fault types were limited to the static state or uniform and/or constant velocity rupture faulting (Boore *et al.*, 1971; Luco and Sotiropoulos, 1985). Using the method proposed in this study, the directivity phenomena could be reproduced in time domain. Hence, some limitations of source approximation were released using numerical modeling. For example, the directivity effects from complex fault ruptures such as slip directions, rupture velocities and complex slip offset could then be studied. The major objective of this study was to develop a modeling technique to theoretically interpret suitable wave form features observed in the recorded seismograms. In

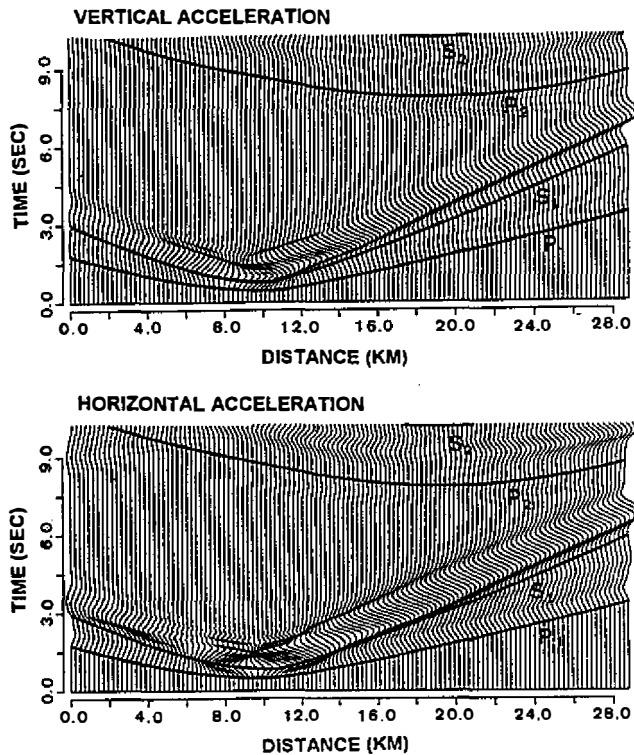


Fig. 14. Horizontal and vertical component synthetic acceleration seismograms for a thrust fault with a uniform rupture velocity (0.8 S-wave velocity) from point B of Figure 11 downward propagating to point A.  $P_1$ ,  $S_1$  are the P-wave and S-wave which radiated from point B;  $P_2$ ,  $S_2$  are the P and S-waves from point A. Identification symbols remain the same as in Figure 12.

this study, the characteristics of the near-source ground motion resulting from the simple two-dimensional dislocation models were examined. The wave form complexity has been effectively analyzed from the forward modeling using the finite element method. Many phases can be traced from the seismic profiles and snapshots via numerical computation. The application of the computer program which was developed by this study was successful in the case the May 20, 1985 Hualien earthquake. Wu (1990) and Tai (1990) employed this method to model the strong motion records of mainshock and aftershocks at station Hualien. The comparison of the calculated and observed motions showed that the characteristics of the fault rupture such as slip amount, direction and rupture propagation direction, velocity and rise time were examined from the wave form modeling (Wu, 1990; Tai, 1990).

In the last few years, although a number of near-source earthquake ground motion records have been obtained, the recorded data are not still sufficient to obtain the relative ground motion in the near-source region. Actually, it is hard to analyze the characteristics of complex fault ruptures such as the change of slip velocity, amplitude and rupture directions from a few recorded seismograms. However, as the quality and quantity of seismic recordings increase, seismologists will be able to improve their ability to identify and interpret complex

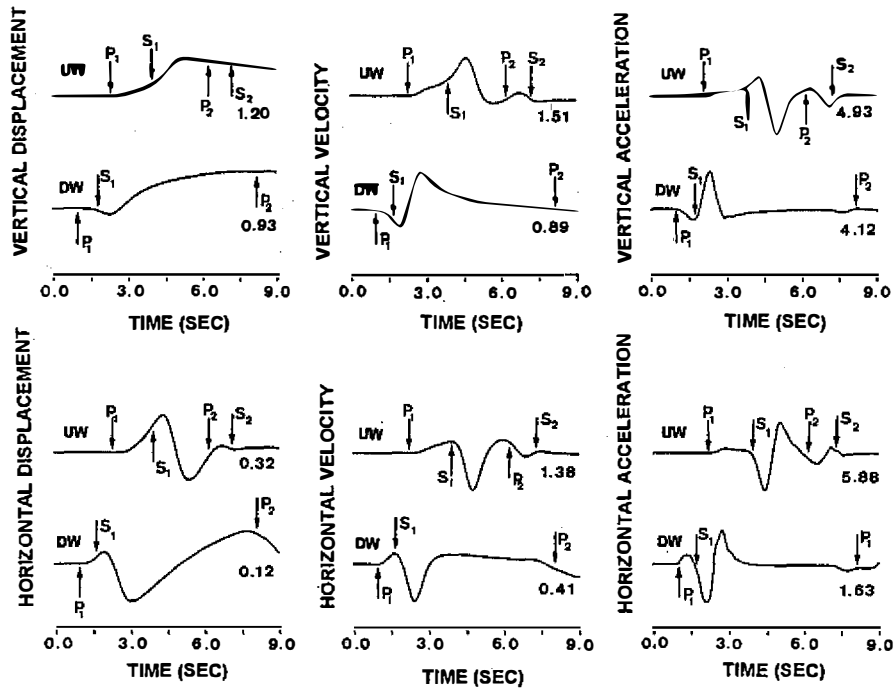


Fig. 15. Comparison of synthetic acceleration, velocity and displacement seismograms from the fault model (Figure 11) on point MP with a uniform upward (UW) and downward (DW) propagating rupture. Both rupture models had the same rupture velocity (0.8 S-wave velocity). Identification symbols remain the same as in Figure 12.

wave forms as functions of structure and source properties from recorded data. The theoretical development and numerical simulation of the near-source ground motion properties are necessary for better understanding of the characteristics of the near-source earthquake ground motion.

Finally, the authors wish to point out that although there are many potential applications, the split node technique, which is employed in this study, is still limited by its infinite fault width assumption. Thus, only the dip-slip fault can be simulated using the 2-dimensional elastic wave equation and most records observed are not dip-slip fault. The application of this method to the modeling of the ground motion is therefore limited. Some extensions are necessary.

## 5. CONCLUSIONS

A method to compute the near field ground motion of a moving dislocation rupture was presented. This method has the ability to model complex rupture directivity. The near-source ground motion features from the complex rupture model such as directivity, starting phase, stopping phase and rupture passing phase were successfully simulated. Results showed the near-source ground motion was strongly affected by propagating rupture process. In short,

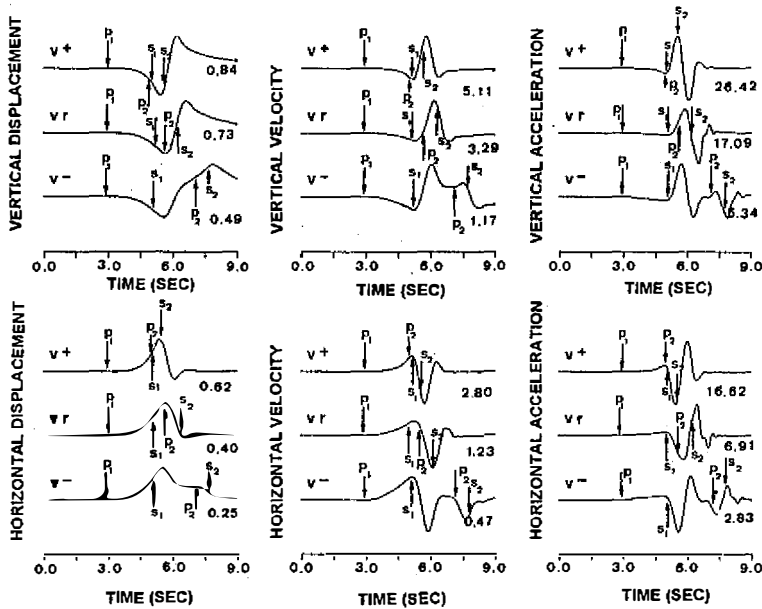


Fig. 16. Comparison of synthetic acceleration, velocity and displacement seismograms from the upward propagation faulting on point L1 of Figure 11 with variable rupture velocities. Identification symbols remain the same as in Figure 13.

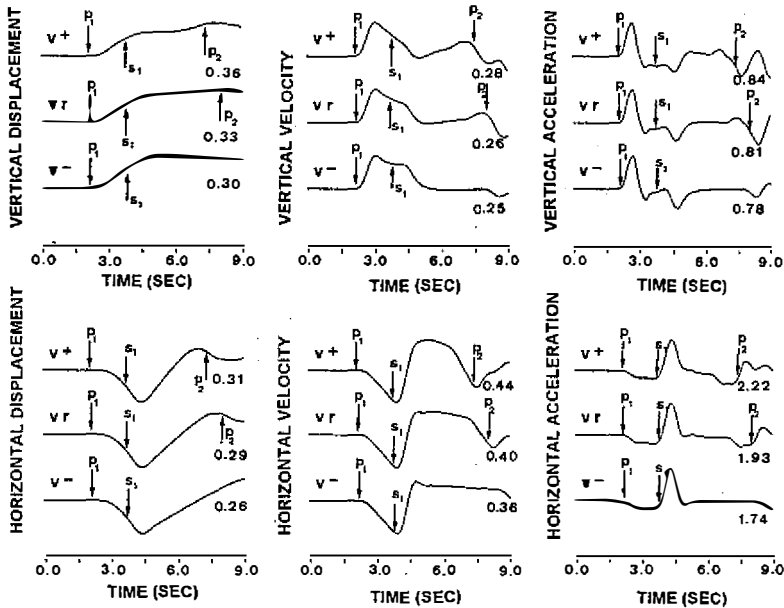


Fig. 17. Comparison of synthetic acceleration, velocity and displacement seismograms from the upward propagation faulting on point R1 of Figure 11 with variable rupture velocities. Identification symbols remain the same as in Figure 16.

for a systematic study of the source rupture process, the finite element method is a useful tool.

**Acknowledgments** This study was supported by Academia Sinica, and the National Science Council, ROC under Grant NSC 82-0202-M-001-098 and NSC 83-0202-M-001-040. The authors also thank two anonymous reviewers for valuable comments.

## REFERENCES

- Abrahamson, N. A., B. A. Bolt, R. B. Darragh, J. Penzien, and Y. B. Tsai, 1987: The SMART-1 accelerograph array (1980-1987): A review. *Earthquake Spectra*, **3**, 263-287.
- Aki, K., 1968: Seismic displacement near a fault. *J. Geophys. Res.*, **73**, 5359-5376.
- Aki, K., and P. G. Richards, 1980: Quantitative Seismology: Theory and Methods. Freeman, San Francisco, California.
- Ammon, C. J., A. A. Velasco, and T. Lay, 1993: Rapid estimation of rupture directivity: application to the 1992 Landers (Ms=7.4) and Cape Mendocino (Ms=7.2), California earthquakes. *Geophys. Res. Lett.*, **20**, 97-100.
- Archuleta, R. J., and G. A. Frazier, 1978: Three-dimensional numerical simulations of dynamic faulting in a half-space. *Bull. Seism. Soc. Am.*, **68**, 541-572.
- Archuleta, R. J., 1984: A faulting model for the 1979 Imperial Valley earthquake. *J. Geophys. Res.*, **89**, 4559-4585.
- Benz, H. M., and R. B. Smith, 1987: Kinematic source modeling of normal-faulting earthquakes using the finite element method. *Geophys. J. R. Astr. Soc.*, **90**, 305-325.
- Boore, D. M., K. Aki, and T. Todd, 1971: A two-dimensional moving dislocation model for a strike-slip fault. *Bull. Seism. Soc. Am.*, **61**, 177-194.
- Boore, D. M., and M. D. Zoback, 1974: Near-field motions from kinematic models of propagating faults. *Bull. Seism. Soc. Am.*, **64**, 321-342.
- Bouchon, M., 1980: The motion of the ground during an earthquake 1. The case of strike slip fault. *J. Geophys. Res.*, **85**, 356-366.
- Bullen, K. E., and B. A., Bolt, 1985: An Introduction to the Theory of Seismology. 4th ed., Cambridge University Press, Cambridge, England.
- CDMG, 1989: Second quick report on CSMIP strong-motion records from the October 17, 1989 earthquake in the Santa Cruz Mountains, October 25, 1989.
- Chiou, S. J., 1991: Estimation of seismic source processes using strong motion array data. PH.D. Dissertation, University of California, Berkeley.
- Douglas, A., J. A. Hudson, and R. G. Pearce, 1988: Directivity and the Doppler effect. *Bull. Seism. Soc. Am.*, **78**, 1367-1372.
- Goldstein, P., and R. J. Archuleta, 1991: Direct measurements of rupture propagation during earthquakes using a dense array: Data analysis. *J. Geophys. Res.*, **96**, 6187-6198.
- Hasegawa, H. S., 1974: Theoretical synthesis and analysis of strong motion spectra of earthquakes. *Canadian Geotech. J.*, **11**, 278-297.

- Haskell, N. A. 1964: Total energy and energy spectral density of elastic wave radiation from propagating faults. *Bull. Seism. Soc. Am.*, **54**, 1811-1841.
- Haskell, N. A., 1969: Elastic displacements in the near-field of a propagating fault. *Bull. Seism. Soc. Am.*, **58**, 865-902.
- Hartzell, S., and T. H. Heaton, 1983: Inversion of strong ground motion and teleseismic waveform data for the fault rupture history of the 1979 Imperial Valley, California, earthquake. *Bull. Seism. Soc. Am.*, **73**, 1553-1558.
- Hartzell, S., 1989: Comparison of seismic waveform inversion results for the rupture history of a finite fault: application to the 1986 North Palm Spring, California earthquake. *J. Geophys. Res.*, **94**, 7515-7534.
- Helmberger, D., D. Dreger, R. Stead, and H. Kanamori, 1993: Impact of broadband seismology on the understanding of strong motions. *Bull. Seism. Soc. Am.*, **83**, 830-850.
- Huang, B. S., 1989: Modeling seismic source geometry and rupture processes by the finite element method. PH. D. Thesis, NCU.
- Huang B. S., and Y. T. Yeh, 1991: Numerical modeling of wave propagation effects by the pseudo-spectral method. Proc. Third Taiwan Symposium on Geophysics, 34-46.
- Huang B. S., and Y. T. Yeh, 1991: Finite element reverse time image for earthquake sources and scatterers. *TAO*, **2**, 17-33.
- Huang, B. S., 1992: Application of 2-D finite element computation to 3-D Green's function synthesis. Proc. Fourth Taiwan Symposium on Geophysics, 11-22.
- Johnson, L. R., 1974: Green's function for Lamb's problem. *Geophys. J. R. Astr. Soc.*, **37**, 99-131.
- Kanamori, H., E. Hauksson, and T. Heaton, 1991: TERRAScope and CUBE project at Caltech. *EOS*, **72**, p.564.
- Luco, J. E. and D. A. Sotiropoulos, 1985: On a decomposition of near-source earthquake motion. *Soil Dynamics and Earthquake Engineering*, **4**, 210-220.
- Madariaga, R., 1976: Dynamics of an expanding circular fault. *Bull. Seism. Soc. Am.*, **66**, 639-666.
- Melosh, H. J., and A. Raefsky, 1981: A simple and efficient method of introducing faults into finite element calculation. *Bull. Seism. Soc. Am.*, **71**, 1391-1400.
- Smith, W. D., 1974: A nonreflecting plane boundary for wave propagation problems. *J. Comp. Phys.*, **15**, 492-503.
- Tai, W. D., 1990: Analysis of the Fault rupture processes of the May 20, 1986 Hualien, Taiwan earthquake by the finite element method. M.S. Thesis, National Central University, 71pp.
- Wald, D. J., D. V. Helmberger, and T. H. Heaton, 1991: Rupture model of the 1989 Loma Prieta earthquake from the inversion of strong-motion and broadband teleseismic data. *Bull. Seism. Soc. Am.*, **81**, 1540-1572.
- Wu, C. F., 1990: Modeling strong ground motion by combining finite element and statistic methods. M.S. Thesis, National Central University, 76pp.
- Wylie, C. R., 1975: *Advanced Engineering Mathematics*. McGraw-Hill, Inc, 937p.
- Yeh, Y. T., and B. S. Huang, 1986: Finite element analysis of coseismic land deformation for seismic source parameters. Proc. First Taiwan Symposium on Geophysics, 19-39.
- Zienkiewicz, O. C., 1977: *The finite element method* (3rd ed.). McGraw-Hill, Berhshire, 787pp.